Received: 4 December 2018 | Revised: 28 July 2019 | Accepted: 29 August 2019

DOI: 10.1002/jbm.b.34489

ORIGINAL RESEARCH REPORT

Layer-by-layer films based on catechol-modified polysaccharides produced by dip- and spin-coating onto different substrates

Ana C. Almeida[1,2] | Ana C. Vale[1,2] | Ricardo A. Pires[1,2,3] | Rui L. Reis[1,2,3] | Natália M. Alves[1,2]

[1]3Bs Research Group, I3Bs—Research Institute on Biomaterials, Biodegradables and Biomimetics, University of Minho, Headquarters of the European Institute of Excellence on Tissue Engineering and Regenerative Medicine, Barco, Guimarães, Portugal

[2]ICVS/3B's PT Associate Laboratory, Guimarães, Portugal

[3]The Discoveries Centre for Regenerative and Precision Medicine, Headquarters at University of Minho, Barco, Guimarães, Portugal

Correspondence
Ana C. Vale and Natália M. Alves, I3Bs—Research Institute on Biomaterials, Biodegradables and Biomimetics, University of Minho, Headquarters of the European Institute of Excellence on Tissue Engineering and Regenerative Medicine, Avepark, 4805-017 Barco, Guimarães, Portugal.
Email: catarina.vale@i3bs.uminho.pt (A. C. V.) and nalves@i3bs.uminho.pt (N. M. A.)

Funding information
Fundação para a Ciência e a Tecnologia, Grant/Award Numbers: MIT-EXPL/BIO/0089/2017, PTDC/BTM-MAT/28123/2017, PTDC/NAN-MAT/31036/2017; H2020 European Institute of Innovation and Technology, Grant/Award Numbers: 668983-FORECAST, 692333-CHEM2NATURE, 739572-THE DISCOVERIES CTR; H2020 Marie Skłodowska-Curie Actions, Grant/Award Number: 778078-REMIX

Abstract

Layer-by-layer films based on chitosan and hyaluronic acid were produced by dip- and spin-coating techniques onto glass, 316L stainless steel and titanium. These natural polymers were modified with catechol groups, in order to build coatings with improved adhesive properties. Polymeric coatings were exclusively composed by both modified polymers whereas the multifunctional coatings combined an inorganic phase of bioactive glass nanoparticles with the polymeric layers to confer bioactivity. Ultraviolet–visible spectroscopy demonstrated that both polymers were successfully synthesized. Fourier transform infrared imaging was used as an innovative way to analyze the layer interdiffusion in these coatings. Their morphology was analyzed by scanning electron microscopy and atomic force microscopy, and their wettability was evaluated by water contact angle measurements. Major differences were found in the structure and surface properties of the coatings assembled either by dip- or spin-coating. The spin-coated films onto glass were smoother, with a more homogeneous structure and lower interdiffusion of polyelectrolytes layers, when compared with the dip-coated ones. Furthermore, it was concluded that the intrinsic surface roughness of stainless steel and titanium substrates had great influence on the surface morphology and wettability of the coatings obtained from both layer-by-layer methodologies.

KEYWORDS
bioactive glass nanoparticles, catechol groups, dip-coating, layer-by-layer, spin-coating

1 | INTRODUCTION

Biomedical metals such as titanium (Ti) and its alloys, 316L stainless steel (SS), and cobalt-chromium (CoCr) alloys have been widely used in orthopedic and maxillofacial applications (Goodman, Yao, Keeney, & Yang, 2013; Niinomi, Nakai, & Hieda, 2012). However, there are still few examples where they have been used successfully in clinic or have reported good in vivo biocompatibility (Xiao, Chen, Biao, Zhang, & Yang, 2017). Therefore, for an effective bone healing, orthopedic prosthesis and their components must present not only adequate mechanical properties, but also important biological functions, such as bioadhesiveness, bioactivity, and biocompatibility (Gittens,

Olivares-Navarrete, Schwartz, & Boyan, 2014; Goodman et al., 2013; Xiao et al., 2017). Current trends for improving osseointegration of orthopedic implants comprise their surface modification with calcium phosphate-like coatings such hydroxyapatite (Mohseni, Zalnezhad, & Bushroa, 2014; Surmenev, Surmeneva, & Ivanova, 2014) or other coatings containing bioactive glasses, for example, 45S5 Bioglass® (Baino, Novajra, Miguez-Pacheco, Boccaccini, & Vitale-Brovarone, 2016; Jones, 2013; Jones, 2015), or biomolecules such as proteins (Korn et al., 2014; Sartori et al., 2015), growth factors (La et al., 2014; Nyberg, Holmes, Witham, & Grayson, 2016; Shah et al., 2014), RGD peptides (Chien, Liu, Kuo, Wang, & Tsai, 2013; Chien & Tsai, 2013; Ryu, Park, Kim, Jeong, & Huh, 2013), and DNA molecules (Dupont et al., 2012). However, these approaches still have significant limitations and drawbacks (Tobin, 2017).

Addressing to these important features, two new biocompatible layer-by-layer (LbL) coatings for orthopedic applications were characterized in this work: multifunctional (MF) and polymeric (CTR) coatings. MF coatings combined adhesion and bioactive properties and were designed to promote bone–implant interaction, as an alternative to bone cements. On the other hand, CTR coatings with enhanced adhesive properties were designed to improve the adhesion between orthopedic implants and other tissues where bioactivity is not a requirement, for instance as an alternative to synthetic tissue adhesives.

Both coatings were composed by natural polymers, chitosan (CHT) and hyaluronic acid (HA) due to their properties, such as biocompatibility, biodegradability, availability, processing and modification flexibility, among others (Kim, Kim, Ryu, & Lee, 2015; Lee et al., 2008; Xu, Strandman, Zhu, Barralet, & Cerruti, 2015). Inspired by the mussel's adhesive proteins (MAPs) (Lee, Scherer, & Messersmith, 2006; Wilker, 2010; Yu & Deming, 1998), both polysaccharides were catechol-functionalized to induce enhanced adhesive properties. So far, our group only demonstrated the adhesive properties of LbL coatings based on CHT and catechol-conjugated hyaluronic acid (HA-C) (Neto et al., 2014; Rego, Vale, Luz, Mano, & Alves, 2016). Since it was demonstrated that the HA-C had a positive effect on their adhesive properties, it was hypothesized that the modification of both polysaccharides could further improve both the adhesive ability and the cytocompatibility of these biomimetic coatings.

Furthermore, based on the interesting osteoconductive properties of bioactive glass nanoparticles (BGNPs) in the orthopedic field (Boccaccini et al., 2010; De, Ghosh, & Rotello, 2008; Mačković et al., 2012), they were used in this work as the inorganic phase of the MF coatings.

Among the different processing techniques proposed to develop nanostructured coatings, LbL deposition appears as one of the most attractive techniques (Alves, Pashkuleva, Reis, & Mano, 2010; Gribova, Auzely-Velty, & Picart, 2012). Several LbL methods have been reported in the literature, including dip-coating, spin-coating, spraying, and perfusion (Borges & Mano, 2014). The dip-coating is the most commonly used due to its simplicity and the low-cost, as well as its suitability to coat substrates with complex geometries (Borges & Mano, 2014; Halasz, Grozdits, & Csóka, 2015). However, since this methodology is time-consuming and requires a relatively large amount of materials for each deposition step, alternative methods should be considered. Spin-coating appears as a good alternative to quickly produce uniform thin films, using the same materials of the dip-coating and allowing electrostatic self-assembly (de Villiers, Otto, Strydom, & Lvov, 2011; Halasz et al., 2015).

In the present work, both CTR and MF coatings were produced onto glass, and also, 316L, SS and Ti substrates by two different LbL deposition methods: dip- and spin-coating. It was the first time that both CHT and HA modified with catechol groups, combined or not with BGNPs, were used to construct LbL coatings onto different substrates and by these two LbL methods. Previous works from our group (Carvalho et al., 2016; Neto et al., 2014; Rego et al., 2016) only used the dip-coating method to construct LbL coatings, based on CHT, HA-C and BGNPs, onto glass substrates. Preliminary results of our group for CTR and MF coatings onto glass substrates with catechol-modified polymers (CHT-C and HA-C) and BGNPs revealed interesting adhesive, bioactive and cellular viability properties. Herein, the surface properties of these innovative biomaterial surfaces obtained through two LbL methods onto different substrates were analyzed. In fact, it is possible to control cell behavior through the surface topography (Alves et al., 2010), so the present work is focused on the influence of the surface roughness and wettability of these two LbL configurations produced onto three substrates, envisaging their orthopedic application. In particular, as far as we know, this is the first time that the polyelectrolyte interdiffusion of LbL coatings was analyzed by FT-IR spectroscopy imaging (chemical maps), which compiles chemical information at a specific location within samples.

2 | MATERIALS AND METHODS

2.1 | Materials

Medium molecular weight chitosan (CHT, viscosity 200–800 cP, Mw = 190–310 kDa, 75–85% N-deacetylation degree), hyaluronic acid sodium salt from *Streptococcus equi* (HA, Mw = 1500–1800 kDa), dopamine hydrochloride (DN, Mw = 189.64 Da), hydrocaffeic acid (HCA, Mw = 182.17 Da), N-(3-dimethylamino)propyl)-N′-ethylcarbodiimide hydrochloride (EDC, Mw = 191.70 Da), dialysis tubing cellulose membrane (avg. flat width 33 mm), calcium nitrate tetrahydrate ($Ca[NO_3]_2{\cdot}4H_2O$ C_2H_6O, 99%), citric acid monohydrate (99%), ammonium phosphate dibasic ($[NH_4]_2HPO_4$, ≥98%), ethanol absolute, ammonium hydroxide solution (maximum of 33% NH_3), sodium chloride (NaCl), hydrochloric acid (HCl), and polyethylenimine (PEI) were purchased from Sigma–Aldrich (St. Louis, MO). Tetraethyl orthosilicate (TEOS, 99.9%) was purchased from Merck KGaA (Darmstadt, Germany). Acetone and 2-propanol were obtained from VWR International (UK). Sodium hydroxide (NaOH) was purchased from Fisher Chemical (Fisher Scientific UK, Leics, UK) and hydrogen peroxide 30% (wt/vol) was obtained from Panreac AppliChem (Darmstadt, Deutschland). CHT was previously purified by recrystallization. Borosilicate coverglasses (Ø = 18 mm, Agar Scientific, Stansted, UK), Ti (Ø = 18 mm, 99.6%

purity, Goodfellow Metals Ltd, Cambridge, UK), and 316L SS (Ø = 18 mm, Goodfellow Metals Ltd, Cambridge, UK) substrates were used for the deposition of LbL coatings by dip- and spin-coating methods. Ti substrates were manually polished with abrasive discs of P180, P320, P600, and P800 (Struers, France). Prior to deposition, all the substrates were cleaned through a sequence of ultrasonic treatments in different solvents during 15 min to remove surface impurities: acetone, absolute ethanol and finally, ultrapure water; then, the substrates were dried with nitrogen flow.

2.2 | HA-C synthesis

HA-C was synthesized from the procedure proposed by Lee et al. (2008) with some modifications. HA modification with catechol groups was performed through the carbodiimide chemistry using EDC as an activation agent of the carboxyl groups on HA chains. HA solution (1% wt/vol) was prepared in phosphate buffered saline (PBS) solution and the pH was adjusted to 5.5 using 0.5 M HCl or 0.5 M NaOH aqueous solution under magnetic stirring. To limit the oxygen interaction, HA solution was purged with nitrogen for 30 min. Then, 338 mg of EDC and 474 mg of DN were added to the previous solution. The reaction was allowed to continue for 36 hr, and the pH was maintained at 5.5 at 4°C. Unreacted chemicals and urea byproducts were removed by dialysis against an acidic osmotized water solution (pH 5.0, HCl solution) for 4 days and osmotized water for 1 day, using a dialysis membrane tube, at 4°C. Finally, the HA-$C_{36\ hr}$ conjugates were freeze-dried for 4 days and stored at −20°C. The entire procedure and storage of the produced HA-$C_{36\ hr}$ was performed at 4°C and protected from light to prevent oxidation of catechol groups.

2.3 | Catechol-conjugated chitosan (CHT-C) synthesis

CHT-C synthesis was based on the procedure proposed by Kim et al. (2015), Xu et al. (2015), and Ghadban et al. (2016) but with some modifications. As in the HA-C synthesis, the CHT modification with catechol groups was accomplished by the carbodiimide chemistry using EDC as an activation agent. A chitosan solution, 1% (wt/vol), was previously prepared in HCl solution at pH 2.5. Then, a HCA solution, 6% (wt/vol), was prepared in osmotized water and 12% (wt/vol) EDC solution was prepared in a mixture of osmotized water and ethanol. These two previous solutions were mixed and added to the CHT solution, under stirring at 4°C, followed by the addition of 1 M NaOH solution to obtain a final pH of 4.8. The reaction was maintained for 18 hr, under nitrogen atmosphere for 30 min. Subsequently, the resulting CHT-$C_{18\ hr}$ was purified by dialysis against an acidic osmotized water solution (pH 5.0, HCl solution) for 3 days and osmotized water for 4 hr, using a dialysis membrane tube, at 4°C. The modified product was freeze-dried and stored at −20°C. Also, as in the HA-C synthesis, the entire procedure and storage of the produced CHT-C was performed at 4°C and protected from light to prevent oxidation of catechol groups.

2.4 | BGNPs production

The procedure to obtain the ternary system of BGNPs with the composition SiO_2:CaO:P_2O_5 (mol %) = 50:45:5, was based on the sol–gel method already optimized by two previous works (Hong, Reis, & Mano, 2009; Luz & Mano, 2011). Firstly, a "solution A" was prepared through a mixture of precursor's solutions. So, calcium nitrate tetrahydrate, the calcium precursor, was dissolved in osmotized water at room temperature. Then, TEOS, the silica precursor, together with ethanol absolute was added to the previous solution. The pH of solution A was adjusted to 2 with citric acid solution, under magnetic stirring for 3 hr. Simultaneously, a "solution B" was also prepared by adding ammonium phosphate dibasic, the phosphorus precursor, to osmotized water. The pH of solution B was adjusted to 11.5 with ammonia hydroxide solution. Under stirring, the solution A was slowly added, drop-by-drop, to solution B and the pH was maintained at 11.5 by continuous supplement of ammonia hydroxide solution. This reaction mixture was left under stirring during 48 hr and then, under resting for 24 hr to occur the gel particle precipitation. Afterwards, the gel precipitate was washed three times with osmotized water and stored during 24 hr at −80°C to be subsequently freeze dried for 7 days. The obtained white gel powder was calcinated at 700°C for 3 hr to obtain BGNPs with improved bioactivity.

2.5 | UV–Vis characterization of HA-C and CHT-C

Before the construction of the LbL films, the polyelectrolytes used were characterized by UV–Vis to determine their substitution degree, DS (%). A Synergy HT Multi-Mode Microplate Reader (BioTek Instruments) with an absorbance measurement range of 200–350 nm, and a quartz microplate with 96 wells was used. Polymeric solutions with 0.05% (wt/vol) HA-$C_{36\ hr}$, and 0.1% (wt/vol) CHT-$C_{18\ hr}$ were prepared in 0.15 M NaCl for the UV analysis, being 0.15 M NaCl solution used as blank. All experiments were performed at a controlled temperature (25°C), and these results were represented as a mean of three measurements.

2.6 | LbL assembly of the coatings

The LbL assembly of different coatings onto glass, 316L SS and Ti substrates was carried out using the two previously described methods, dip-coating and spin-coating, at room temperature. For such, four different solutions of CHT-$C_{18\ hr}$ (0.1% wt/vol), HA-$C_{36\ hr}$ (0.05% wt/vol), BGNPs (0.25% wt/vol) and PEI (0.5% wt/vol) were prepared with 0.15 M NaCl solution, under magnetic stirring overnight. Except for PEI, the pH of these solutions was adjusted to 5.5 using 0.5 M NaOH or 0.5 M HCl aqueous solutions. To avoid BGNPs agglomeration, suspensions containing these nanoparticles were kept under magnetic stirring and periodically subjected to an ultrasonic treatment during 10–15 min.

HA-$C_{36\ hr}$ and BGNPs were used as polyanion, while CHT-$C_{18\ hr}$ was used as polycation. PEI was used as an initial layer precursor by immersing each substrate for 20 min, prior to multilayer deposition.

Therefore, after immersion in PEI, the polycation CHT-$C_{18\ hr}$ was used to initiate alternated deposition between oppositely charged polyelectrolytes.

Attending some previous findings obtaining by our group for distinct LbL coatings onto glass substrate with CHT-C, HA-C, and BGNPs, the ones with promising adhesive, bioactivity and cellular viability properties (see Supplementary Material) were constructed with 11 bilayers (i.e., 22 layers), as shown in Figure 1: Multifunctional films containing [CHT-$C_{18\ hr}$/HA-$C_{36\ hr}$/CHT-$C_{18\ hr}$/BGNPs]$_5$ + [CHT-$C_{18\ hr}$/HA-$C_{36\ hr}$] (MF); and polymeric films (control) with [CHT-$C_{18\ hr}$/HA-$C_{36\ hr}$]$_{11}$ (CTR). MF films ending with an adhesive layer were chosen, since in a previous work (Rego et al., 2016), it was found that these films had higher adhesive strength than those ending with BGNPs.

Dip-coated films were assembled by alternating substrate immersion in the oppositely-charged polyelectrolytes solutions. The dipping times were established after an optimization process in previous works of our group (Neto et al., 2014; Rego et al., 2016), where 10 min were used for CHT-$C_{18\ hr}$ and HA-$C_{36\ hr}$, and 20 min for BGNPs. In addition, a rinsing step of 5 min with 0.15 M NaCl solution was included between the adsorptions of each polyelectrolyte.

Spin-coated films were prepared using a spin-coater (WS-650Hzb-23NPPB-UD-3, LAURELL) and 300 μl of the polyelectrolytes solution was dropped for the first bilayer, 200 μl for the second bilayer and 100 μl for the remaining bilayers, ensuring that the entire surface area of substrate was covered. Polyelectrolytes solutions were alternatively spin-coated onto the substrates at a spinning speed of 3000 rpm for 10 s and an acceleration of 1300 rpm^2. Additional rising steps between the layer depositions were excluded, since the concentration of polyelectrolytes solutions used was low. At the end of each procedure, these coatings were rinsed three times in ultrapure water and, finally, LbL coatings were dried at room temperature overnight.

2.7 | Surface characterization

The surface morphology of LbL coatings was analyzed by scanning electron microscopy (SEM, JSM-6010 LV, JEOL, Japan) and Fourier transform infrared (FT-IR) imaging (Perkin-Elmer Instruments, Shelton, CT). Before SEM analysis, LbL coatings were sputtered with a thin platinum layer, using a sputter coater EM ACE600 (Leica Microsystems, Germany). SEM microphotographs were taken with a resolution of 500 μm and 10 μm. FT-IR imaging analysis was performed using a Perkin-Elmer Spectrum Spotlight 300 FT-IR Microscope System in reflectance mode. FT-IR maps were constructed by a spectrum collected in continuous scan mode for a spectral range 4000–720 cm^{-1} and sample areas of 500 × 500 μm^2. Each spectrum was collected with an average of 15 repetitive scans with a spectral resolution of 16 cm^{-1}. FT-IR spectra were integrated by taking the areas under the curve between the limits of the peaks of interest. The peak ranges were chosen based on the characteristic peaks corresponding to specific vibrational bonds for all materials constituting the LbL coatings. A false color was assigned to each material analyzed. C═O stretching of amide I centered at approximately 1650 cm^{-1}, was the region chosen for CHT identification, and the C═O stretching of carboxylic acid at about 1730 cm^{-1} was chosen for HA, both depicted on the chemical maps by red and green, respectively (Kennedy, Rio, & Kuo, 2006; Peniche et al., 1999). The characteristic peak of CHT corresponding to the amine deformation vibration, N—H bending vibration, centered at 1590 cm^{-1} could not be used due to overlapping with the amide II peak present in both polysaccharides (Lawrie et al., 2007). On the other hand, the region chosen for catechol groups identification corresponds to out-of-plane C—H bending vibration centered at 740 cm^{-1} and C—H stretching vibration centered at 3052 cm^{-1}, both belonging to the aromatic C—H group and represented on the chemical maps by blue (Altmaier, Kienzler, Montoya, Duro, & Grivé, 2012; Huang, Bao, Liu, Wang, & Hu, 2017; Jha & Halada, 2011). The C═C vibrations peaks of the aromatic ring, approximately between 1466 and 1515 cm^{-1}, were not chosen due to overlapping with characteristic peaks of the polysaccharides (Altmaier et al., 2012; Jha & Halada, 2011). Furthermore, for the BGNPs identification, the chosen region was the one

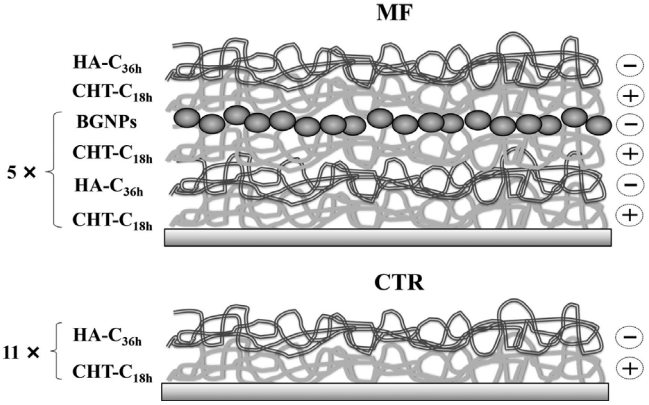

FIGURE 1 Schematic illustration of the multifunctional (MF) and control (CTR) coatings

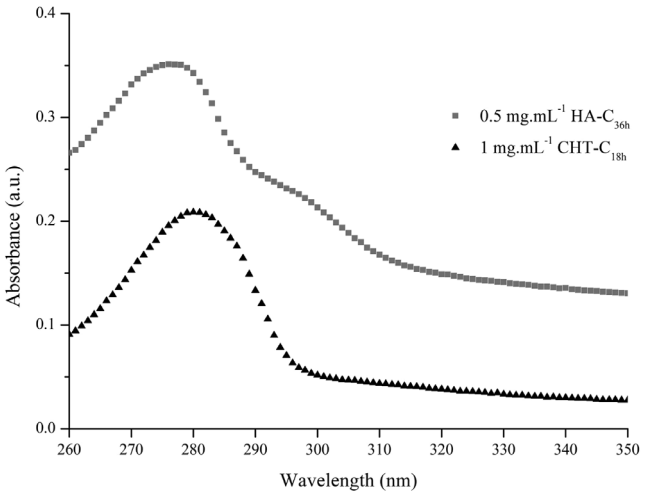

FIGURE 2 UV–vis spectra for HA-$C_{36\ hr}$ and CHT-$C_{18\ hr}$ solutions between 260 and 350 nm

corresponding to the silicate absorption bands, Si—O—Si, assigned to the peaks 1085 and 800 cm^{-1} related to the asymmetric stretching and symmetric stretching vibrations respectively, and represented in the chemical maps by cyan (Luz & Mano, 2011; Ma, Chen, Wang, Meng, & Shi, 2010).

The surface roughness of the LbL coatings was analyzed by atomic force microscopy (AFM) using a JPK NanoWizard III system (JPK Instruments AG, Berlin, Germany). Topographical images of dried LbL coatings were acquired under AC mode in air using silicon probes (ACTA, AppNano; k = 40 N/m), a resolution of 512x512 pixels, a line rate between 0.5 and 1.0 Hz and a resonance frequency of 300 kHz. Triplicate AFM images of $20 \times 20\ \mu m^2$ were used to calculate two parameters of surface roughness: the root-mean-square roughness, R_q, and the arithmetic roughness, R_a.

The surface wettability of LbL coatings was also evaluated by the sessile drop method (Kumar, 2013; Williams, 2011) using an OCA15plus Goniometer equipment (DataPhysics Instruments GmbH, Filderstadt, Germany). For each coated surface, three measurements were performed, using 3 µl droplets of osmotized water. The water contact angle (WCA) measurements were performed at room temperature and the pictures were taken immediately after the drop contacted the surface. Then, the results were treated using the SCA20 software (DataPhysics Instruments GmbH, Filderstadt, Germany).

2.8 | Statistical analysis

The results of all experiments were carried out at least in three replicates (n = 3) and were presented as mean ± standard deviation (*SD*). Statistical significance between groups was determined by One-way ANOVA with Tukey's Multiple comparison test, using Graph Pad Prism version 6.0 (GraphPad software, San Diego, CA). Statistical differences were represented and set to $p < .05$(+/*), $p < .01$(++/**), $p < .001$(+++/***), and $p < .0001$(++++/****).

3 | RESULTS

3.1 | UV–vis analysis of HA-C and CHT-C modified polymers

In order to verify that the modification of HA and CHT with catechol groups was successful, HA-$C_{36\ hr}$ and CHT-$C_{18\ hr}$ solutions were

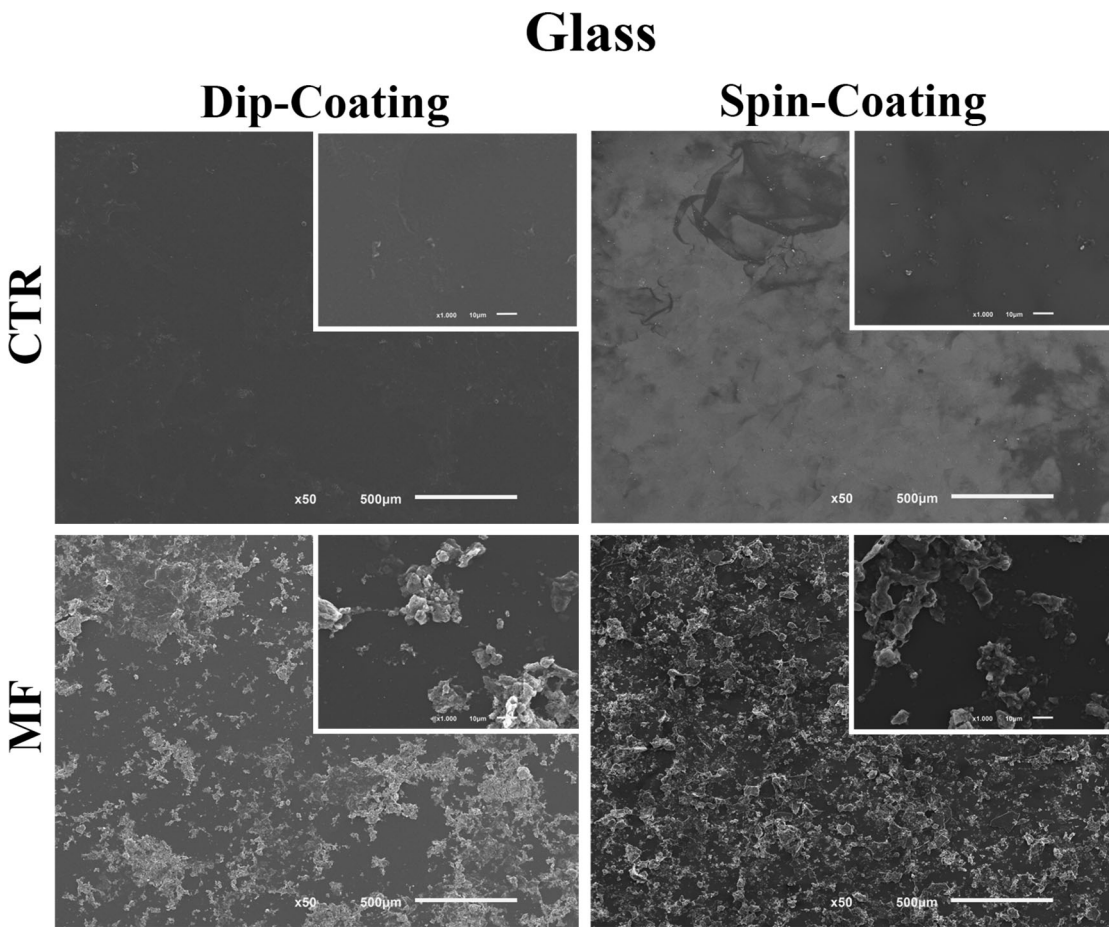

FIGURE 3 SEM images of the two LbL coatings configurations (Figure 1) obtained by dip- and spin-coating, using glass as substrate. The scale bar of the main images represents 500 µm and the secondary ones 10 µm

analyzed by UV–Vis spectroscopy. As Figure 2 shows, the spectra of HA-$C_{36\ hr}$ and CHT-$C_{18\ hr}$ exhibit a maximum absorbance peak at a wavelength around 280 nm.

3.2 | SEM and FT-IR imaging analysis of the coatings

Upon confirmation of the successful modification of the two polymers, dip- and spin-coated LbL films were produced onto distinct substrates, as described in the experimental section. The surface morphology of these coatings was analyzed by SEM. Figures 3–5 show micrographs of the produced coatings using glass, 316L SS and Ti as substrates, respectively. Different morphologies between the surfaces of the dip- and spin-coated LbL films were observed for these three types of substrates. Independently of the substrate, all spin-coated formulations seemed to be smoother and with a more homogeneous structure than the dip-coated ones. MF films evidenced the presence of some particle agglomeration, when compared to CTR films, related to the presence of BGNPs. Moreover, BGNPs distribution at the film surface revealed to be more homogeneous in the spin-coated films than in the dip-coated ones. In addition to these particles, minor ones may be observed in almost all formulations, which we believe to be polymeric agglomerations of the coating components.

To further characterize the surface distribution of the various components of the LbL coatings obtained by dip- and spin-coating, namely CHT, HA, catechol groups and BGNPs, FT-IR imaging spectroscopy was conducted. Figures 6–8 show the FT-IR mapping for the produced LbL coatings using glass, 316L SS and Ti as substrates, respectively.

Figure 6 shows that the CTR and MF spin-coated LbL configurations on the glass substrate appeared to have more uniform and ordered coating structures compared to those obtained by dip-coating. This fact was more evident for the spin-coated CTR condition, where it was possible to identify the main presence of HA (green), which was the end-layer of all coatings, indicating a more ordered coating structure. However, spots of a colored mixture were also detected in both dip- and spin-coated CTR films, probably related to the polymeric agglomeration already evidenced by SEM.

In the case of the dip- and spin-coated MF configurations, the presence of BGNPs (cyan) was easily visualized. Some HA (green) and catechol groups (blue) spots related to the end-layer of the LbL coatings were also observed in these formulations. In contrast to the dip- and spin-coated CTR configurations, the coatings containing BGNPs did not exhibit color-mixed spots. Furthermore, for both spin-coated CTR and MF configurations, a lower intensity difference was

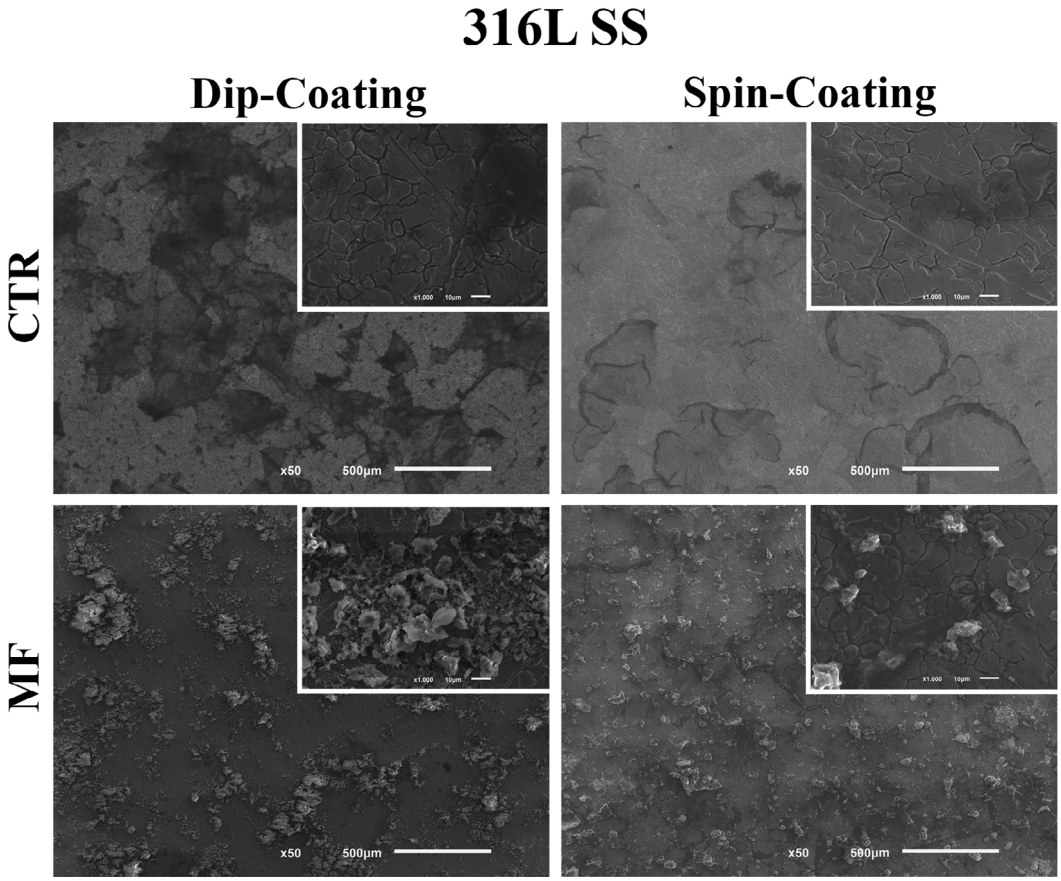

FIGURE 4 SEM images of the two LbL coatings configurations obtained by dip- and spin-coating, using 316L SS as substrate. The scale bar of the main images represents 500 µm and the secondary ones 10 µm

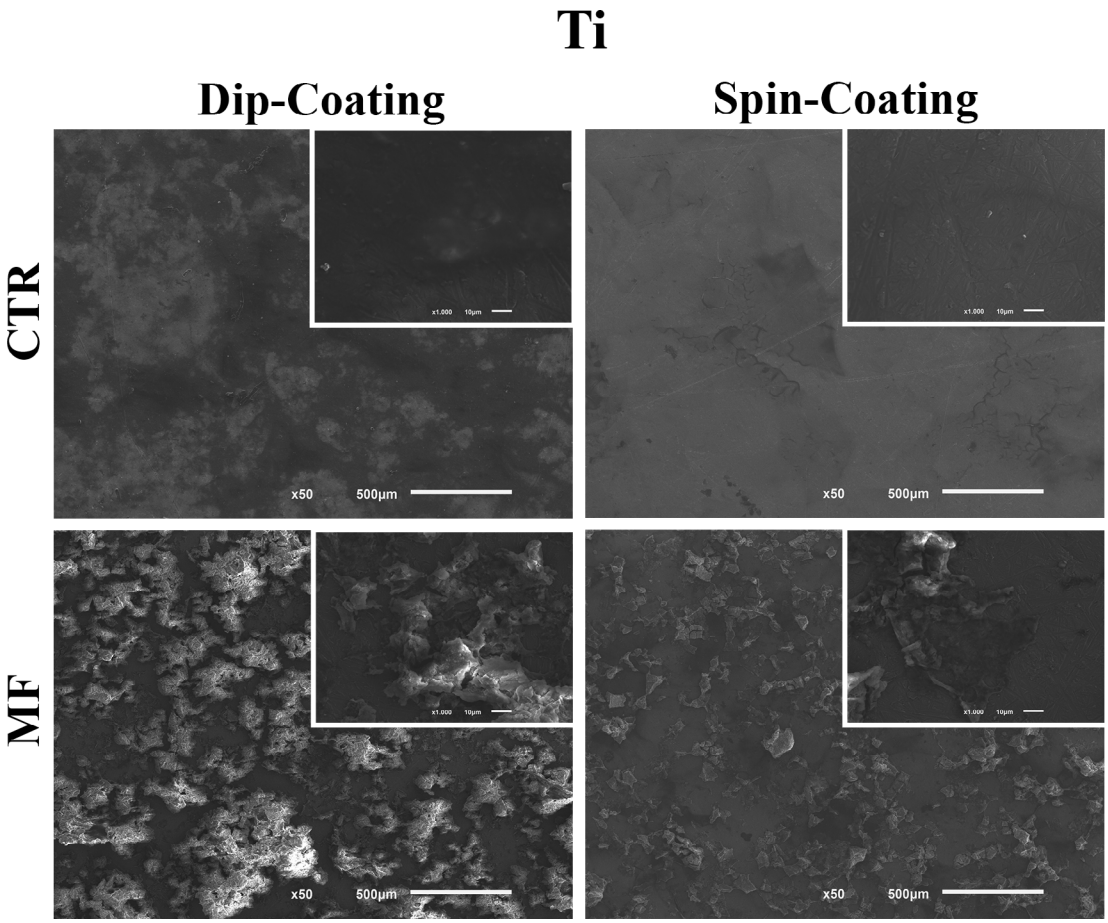

FIGURE 5 SEM images of the two LbL coatings configurations obtained by dip- and spin-coating, using Ti as substrate. The scale bar of the main images represents 500 µm and the secondary ones 10 µm

observed in comparison with the dip-coated ones, which may be an indication of a lower surface roughness.

For both metals, 316L SS and Ti (Figures 7 and 8), these differences were not so obvious. Although differences in intensity were observed between the two LbL methods, a similar color mixture for dip- and spin-coated CTR conditions was noticed. Nevertheless, it was also observed for the metals substrates that the dip- and spin-coated MF films did not present the PE color-mixture, in agreement with the results found for the glass substrate.

3.3 | AFM analysis of the coatings

The topography of the coatings produced onto three substrates was analyzed by AFM. Figures 9–11 show the most representative results obtained for each LbL coating produced on glass, 316L SS and Ti, respectively, by dip- and spin-coating.

Figure 9 shows that the LbL coatings (CTR and MF) obtained by spin-coating presented a statistically significant lower roughness (**** $p < .0001$) than those produced by dip-coating. Moreover, the surface roughness of the MF films containing BGNPs decreases when compared to their respective controls (CTR) (Figure 9), and a similar trend was seen for MF films produced by both LbL assembly methods.

As Figure 10 shows, the SS control exhibited a high surface roughness, with a R_q value around 315 ± 58 nm. Indeed, the SS substrates were used without further surface treatment. Thus, despite some changes in the surface roughness between the LbL conditions and the SS control were noted, due to the presence of the coatings, they are not relevant. Except for the spin-coated MF condition, a tendency to decrease the surface roughness of the LbL conditions compared to the SS control was observed. Although, this decrease was not observed for the spin-coated MF condition, but it should be mentioned that this configuration has a significant standard deviation value (R_q value around 340 ± 147 nm). Furthermore, a slight decrease of the surface roughness of the spin-coated CTR condition was observed when compared to the dip-coated one. Unlike the AFM results of the glass, the presence of BGNPs in both dip- and spin-coated MF film appeared to contribute to a greater surface roughness compared to their respective controls (CTR).

Ti also presented a considerable surface roughness, with R_q value around 125 ± 4 nm (Figure 11), although it was lower than the SS control. So, the roughness differences between Ti substrates and the LbL coatings were not evident. Nevertheless, it seems that CTR films presented a lower roughness than the Ti control, whereas the MF films had a higher roughness. Furthermore, no significant differences

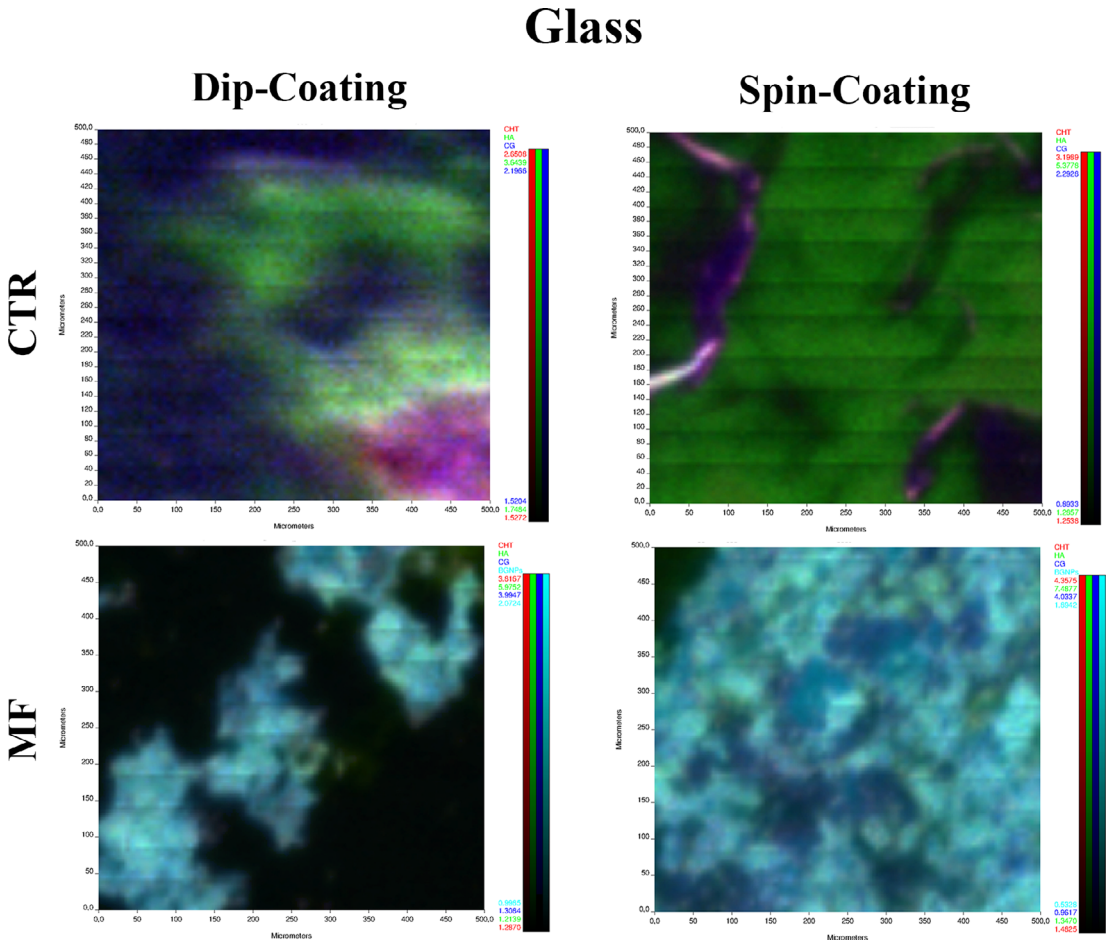

FIGURE 6 Chemical maps of the two LbL coatings configurations (Figure 1) obtained by dip- and spin-coating, using glass as substrate. For the chemical map, red indicates the presence of CHT, green the presence of HA, blue the presence of catechol groups, and cyan corresponds to the BGNPs. Note that the existence of regions with different intensities can be an indication of differences in thickness. Maximum for the scale bars corresponds to 500 μm

between those two LbL techniques were noticed. Also, similar to the 316L SS results, for both dip- and spin-coated MF films, the presence of BGNPs appeared to contribute to a higher surface roughness than for their respective controls.

3.4 | WCA analysis

The wettability of the developed LbL coatings was assessed by WCA analysis (Kumar, 2013; Williams, 2011). Figures 12–14 show the wettability results for each LbL coating produced onto glass, 316L SS and Ti, respectively, by dip- and spin-coating.

As expected from the AFM analysis, WCA changes between the distinct LbL conditions and the glass substrate were noticed (Figure 12). These changes were statistically significant for all conditions obtained by dip- and spin-coating. Moreover, it was found that the coatings produced by both LbL methods exhibited higher hydrophilicity than the glass control (WCA around 74°). Also, the inclusion of BGNPs in the dip- and spin-coated films seemed to affect their wettability. In fact, the presence of BGNPs in the MF films were able to turn their surfaces more hydrophilic, showing lower WCA values in comparison with those obtained for their respective controls. Furthermore, the decrease in WCA values for the dip-coated conditions (CTR and MF) shown statistically significant differences (****, $p < .0001$) in comparison with the spin-coated ones.

WCA varied between the distinct LbL conditions and the SS control (Figure 13). Similarly with the glass wettability results, coatings obtained through both LbL methods showed higher hydrophilicity than the uncoated SS substrate (WCA around 107°). In particular, a statistically significant WCA decrease was detected for the dip- and spin-coated MF conditions, while a less significant decrease was observed for the dip-coated CTR condition. On the other hand, the spin-coated CTR condition showed only a slight WCA decrease. Furthermore, a more pronounced WCA decrease was found for both dip- and spin-coated MF conditions, when compared to their respective controls. Additionally, Figure 13 evidences significant higher WCA values for both spin-coated CTR and MF conditions, when compared to the dip-coated ones.

Once again, WCA variations between the distinct LbL conditions and Ti control were also detected (Figure 14). Unlike glass and SS wettability results, the decrease of WCA was not detected for all

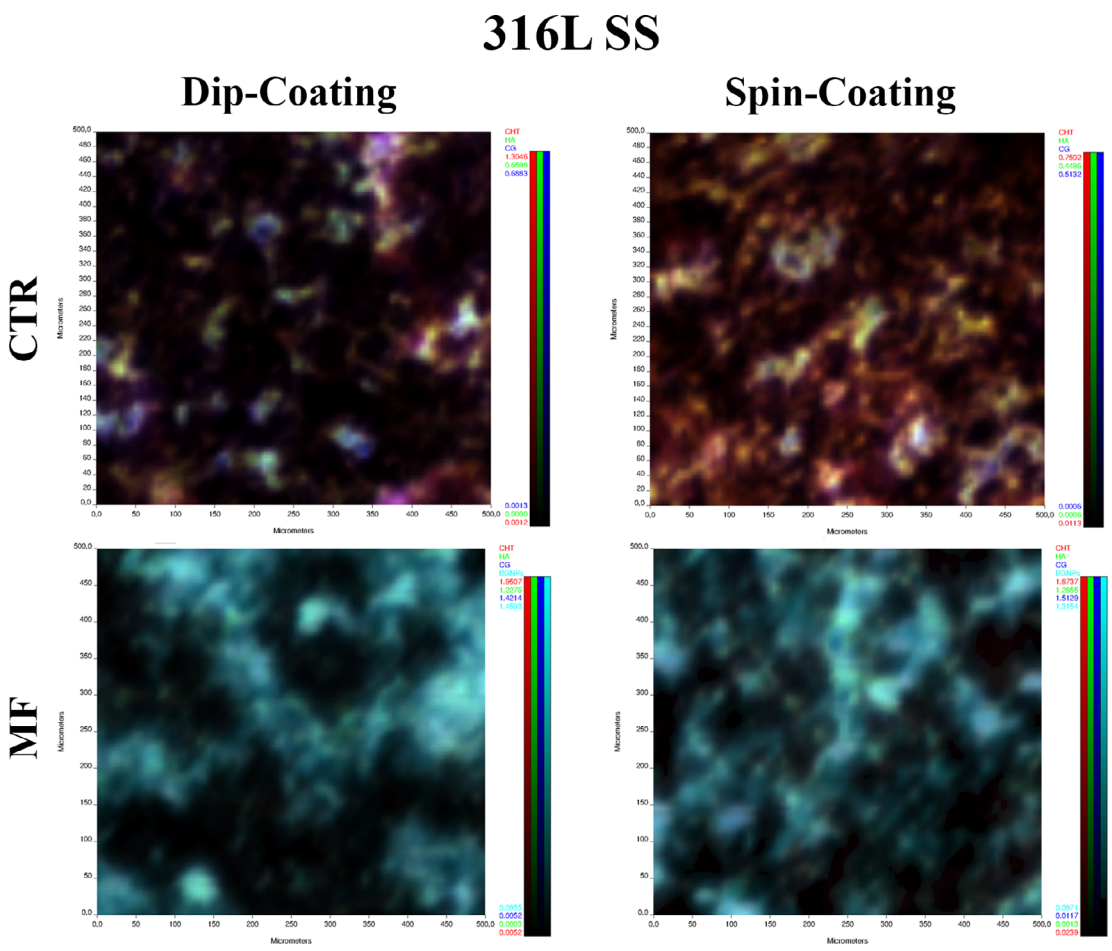

FIGURE 7 Chemical maps of the two LbL coatings configurations obtained by dip- and spin-coating, using 316L SS as substrate

conditions, when compared to the Ti control. In particular, a significant WCA increase was observed for the dip-coated CTR and the spin-coated MF. On the other hand, a significant WCA decrease was detected only for the dip-coated MF. The dip-coated CTR condition shown a significant decrease in the hydrophilicity of the Ti substrate compared to the spin-coated one (Figure 14), showing WCA values similar to the Ti control (WCA values around 61°). On the other hand, the dip-coated MF condition led to a significant increase in the hydrophilicity of the Ti substrates, when compared to the spin-coated one. Furthermore, as it was noticed for glass and SS substrates, a significant WCA decrease was detected for the dip-coated MF, when compared to its respective control.

4 | DISCUSSION

Inspired by the DOPA configuration of MAPs, CHT and HA were modified with catechol groups to induce enhanced adhesive properties of LbL films produced by dip- and spin-coating techniques (Ghadban et al., 2016; Kim et al., 2015; Lee et al., 2008; Xu et al., 2015). UV–Vis analysis (Figure 2) showed a maximum absorbance peak at a wavelength around 280 nm for both HA-$C_{36\ hr}$ and CHT-$C_{18\ hr}$ confirming the presence of the catechol groups in the modified CHT and HA polymers (Kim et al., 2015; Neto et al., 2014; Rego et al., 2016; Xu et al., 2015). Moreover, the absence of additional peaks at wavelengths longer than 300 nm proves that the synthesized conjugates were not oxidized (Kim et al., 2015; Neto et al., 2014; Rego et al., 2016; Xu et al., 2015). According to the experimental values (see Supplementary Material), the DS (%) obtained for HA-$C_{36\ hr}$ and CHT-$C_{18\ hr}$ were around 54% and 11%, respectively. These DS (%) results were different from those found in other works (Ghadban et al., 2016; Kim et al., 2015; Lee et al., 2008; Neto et al., 2014; Rego et al., 2016; Xu et al., 2015). The DS (%) of HA-$C_{36\ hr}$ was higher than the value of 11% obtained in our previous studies (Neto et al., 2014; Rego et al., 2016), and could be explained by the different molecular weight of HA and/or the distinct reaction time. On the other hand, the DS (%) value of CHT-$C_{18\ hr}$ was slightly lower than the one found in other works (Ghadban et al., 2016; Kim et al., 2015; Xu et al., 2015), and could be related with different conditions used in this study, such as the relative proportions of the reagents, the molecular weight of CHT, the reaction time and the fact that the conjugate was dissolved in 0.15 M NaCl.

Upon the build-up of the LbL films on glass, 316L SS and Ti, differences in the morphology between the surfaces of the dip- and spin-coated LbL films were observed by SEM (Figures 3–5). These results demonstrated that, independently of the substrate, the spin-coating process contributes for smoother and more homogeneous LbL films.

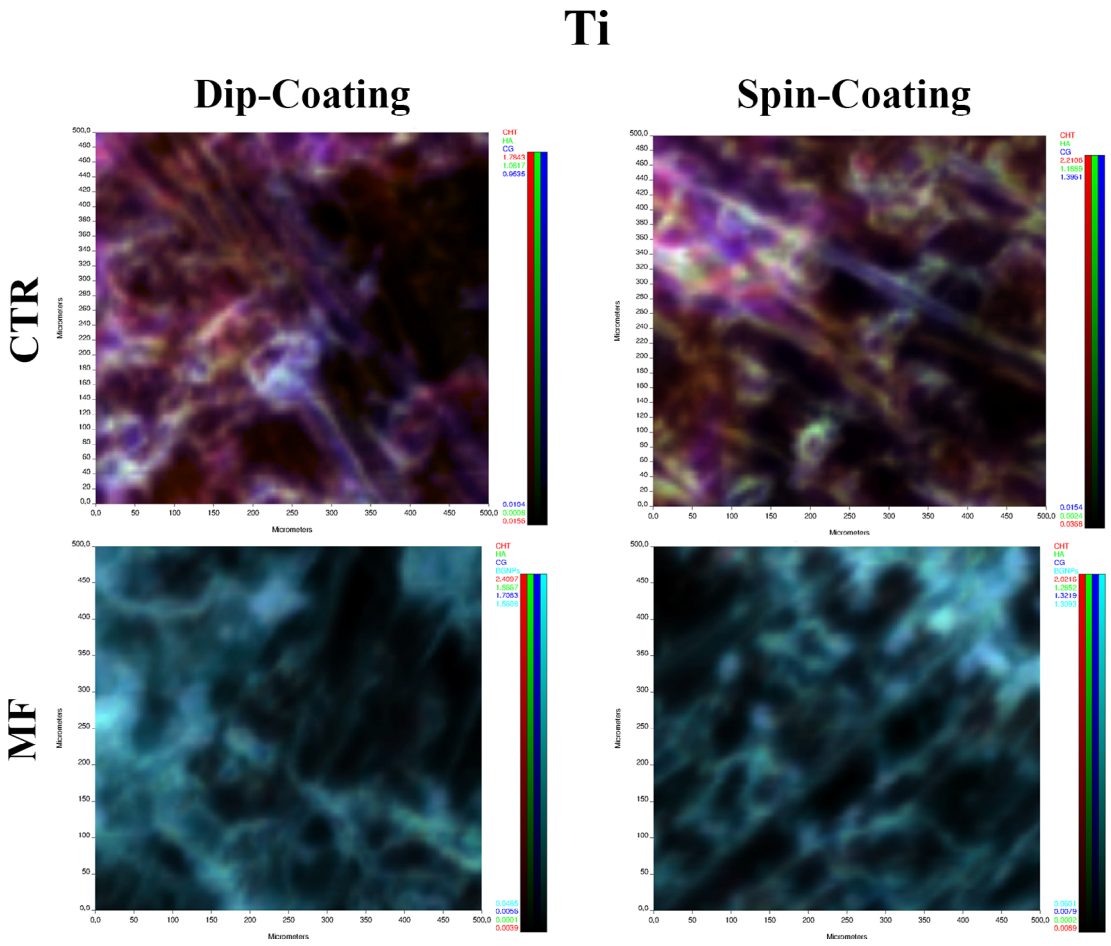

FIGURE 8 Chemical maps of the two LbL coatings configurations obtained by dip- and spin-coating, using Ti as substrate

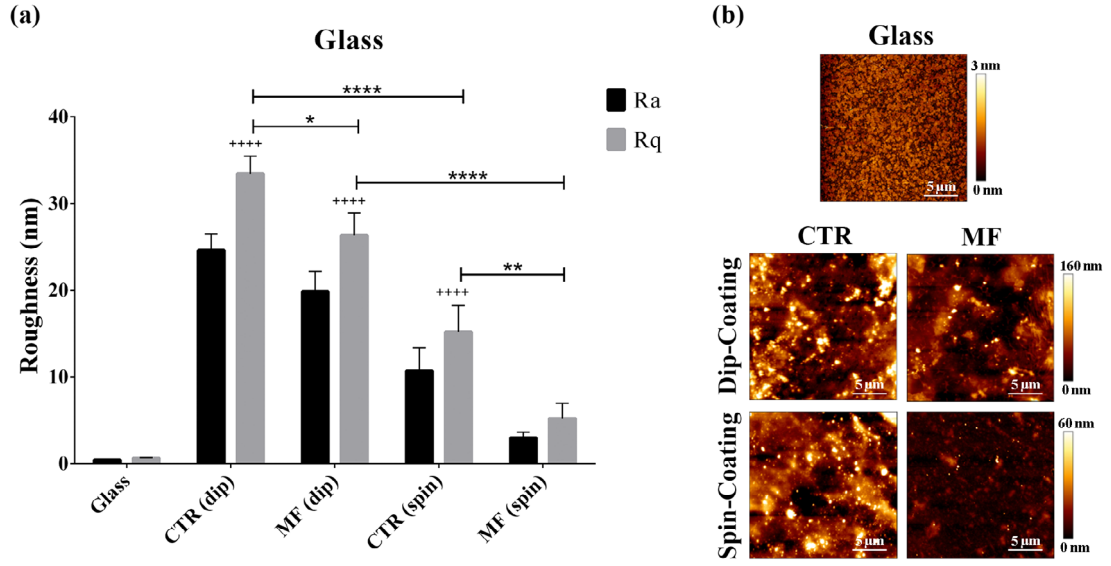

FIGURE 9 (a) R_a and R_q roughness values (nm) measured for the two LbL coatings configurations (Figure 1) produced onto glass by dip- and spin-coating. Data are presented as average ± standard deviation (n = 3). Statistical differences were represented for R_q roughness values, where "*" indicate differences between the various conditions, and "+" (at the top of each bar) indicate their differences compared to the uncoated glass substrate (glass control) [++++/**** p < .0001; ** p < .01; * p < .05; One-way ANOVA with Tukey's Multiple comparison test]. (b) Representative AFM images for each LbL coating condition, with a scanned surface area of 20 × 20 µm^2

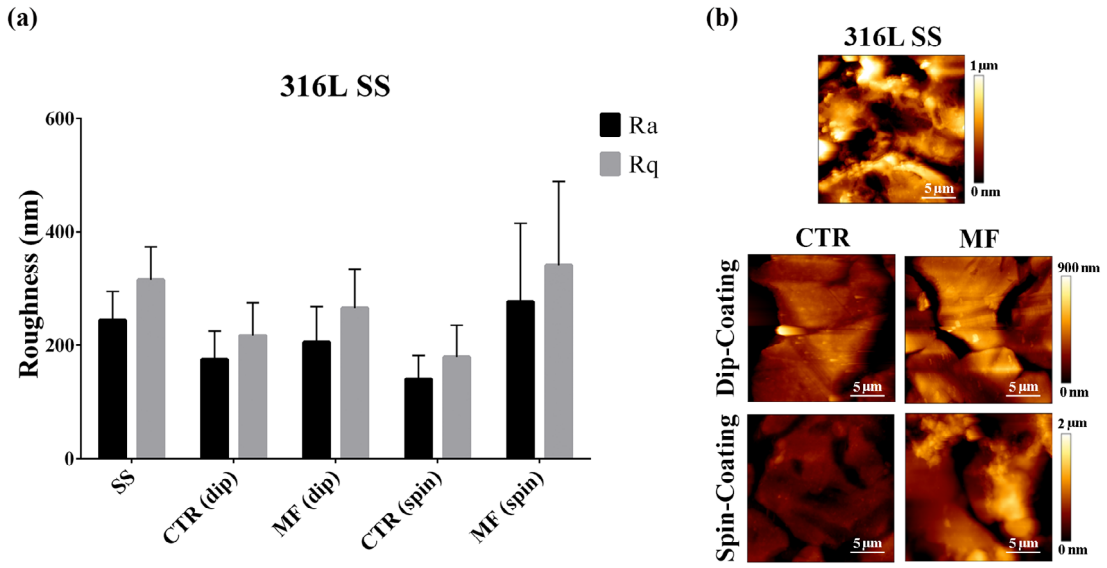

FIGURE 10 (a) R_a and R_q roughness values (nm) measured for the two LbL coatings configurations produced onto 316L SS by dip- and spin-coating. Data are presented as average ± standard deviation (n = 3) (One-way ANOVA with Tukey's Multiple comparison test). (b) Representative AFM images for each LbL coating condition, with a scanned surface area of 20 × 20 µm^2

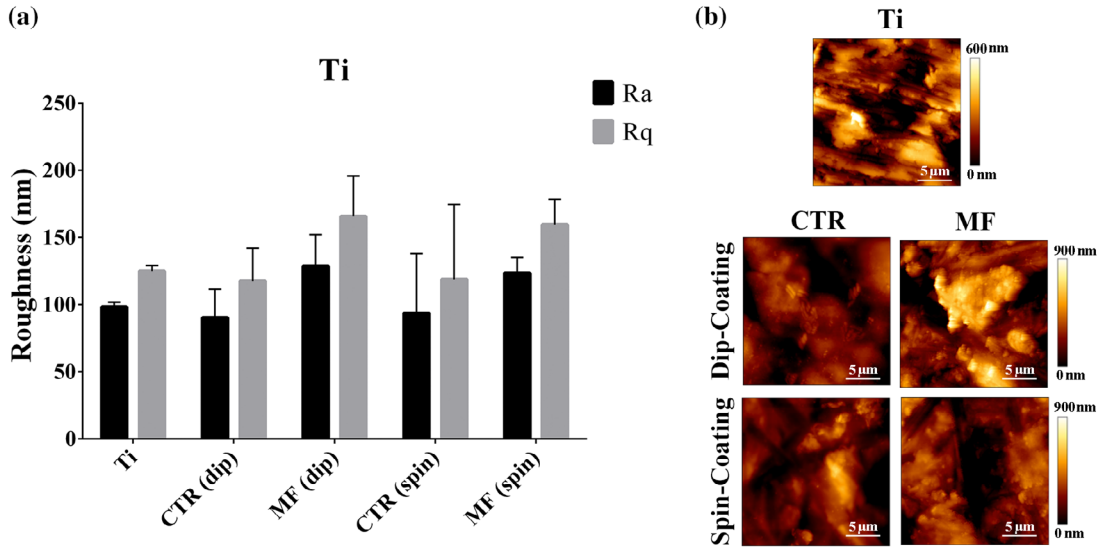

FIGURE 11 (a) R_a and R_q roughness values (nm) measured for the two LbL coatings configurations produced onto Ti by dip- and spin-coating. Data are presented as average ± standard deviation (n = 3) (One-way ANOVA with Tukey's Multiple comparison test). (b) Representative AFM images for each LbL coating condition, with a scanned surface area of 20 × 20 µm^2

Herrera, Sirviö, Mathew, and Oksman (2016) observed the same for nanocellulose coatings on porous cellulose substrates produced by both dip- and spin-coating. They found that the coating thickness was hundreds of nanometers for the spin-coated films, whereas for the dip-coated ones was in the micrometers range (Herrera et al., 2016).

Moreover, it was believed that the centrifugation step in the spin-coating method, or the interlayer diffusion of polyelectrolytes in the dip-coating method, gave rise to the presence of polymeric agglomerations of the coating components that were not completely removed (Marudova et al., 2016). In fact, dip-coated films have demonstrated to present more polyelectrolyte interpenetration between the layers than spin-assisted films contributing to an exponential growth of film thickness and less ordered structures (Cho, Char, Hong, & Lee, 2001; Lee et al., 2009; Marudova et al., 2016). In addition, the exponential growth is usually observed for weakly charged PEM systems and can be attributed to the reversible interdiffusion of at least one of the polyelectrolyte species that constitute the film (Marudova et al., 2016). In order to confirm this feature, the surface distribution of various components of the dip- and spin-coated films, namely CHT, HA, catechol groups and BGNPs, was analyzed by FT-IR imaging spectroscopy. Figure 6 showed that the spin-coating process contributed to LbL films with more uniform and ordered coating structures compared to those obtained by

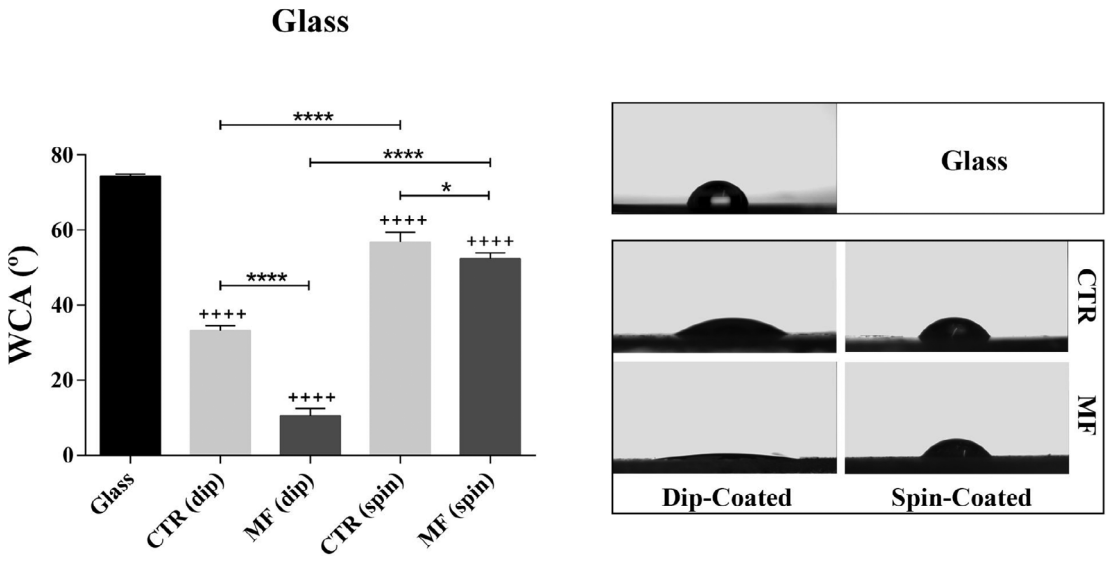

FIGURE 12 (a) WCA (°) values measured for the two LbL coatings configurations (Figure 1) produced onto glass by dip- and spin-coating. Statistical differences between the various configurations are indicated by "*," while their comparisons with the uncoated glass substrate (glass control) are indicated by "+" (at the top of each bar). Data are presented by means ± standard deviation (n = 3; ++++/**** p < .0001; * p < .05) (One-way ANOVA with Tukey's Multiple comparison test); (b) representative image of water drops for each multilayered film surface

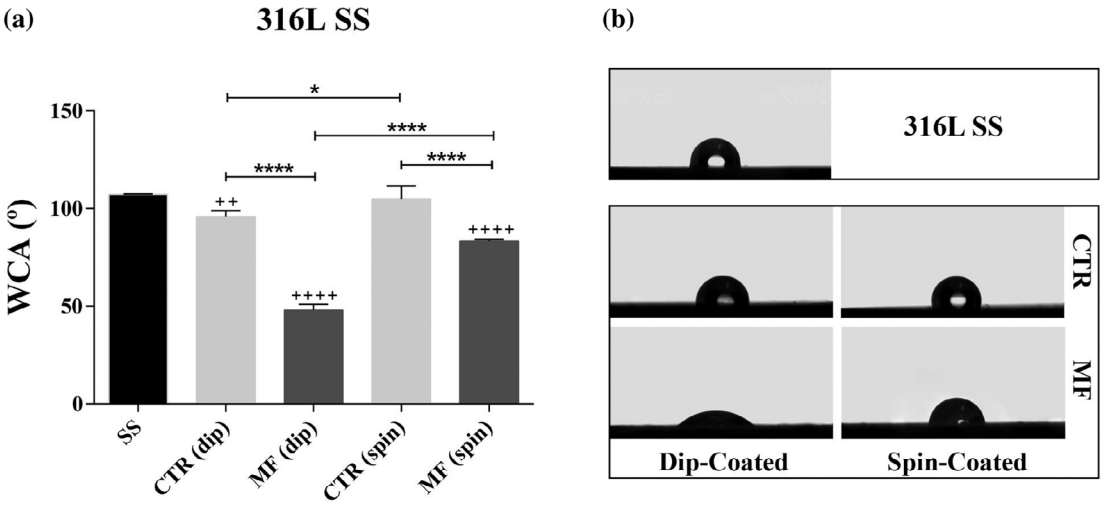

FIGURE 13 (a) WCA (°) values measured for the two LbL coatings configurations produced onto 316L SS by dip- and spin-coating. Statistical differences between the various configurations are indicated by "*," while their comparisons with the uncoated SS substrate (SS control) are indicated by "+" (at the top of each bar). Data are presented by means ± standard deviation (n = 3; ++++/**** p < .0001; ++ p < .01; * p < .05) (One-way ANOVA with Tukey's Multiple comparison test); (b) representative image of water drops for each multilayered film surface

dip-coating, using glass as the substrate. This finding was in agreement with some previous observations (Cho et al., 2001; Lee et al., 2009). Cho et al. (2001) prepared spin- and dip-coated poly(allylamine hydrochloride)/poly(sodium 4-styrenesulfonate) films and the AFM analysis evidenced highly ordered structures for the spin-coated ones. Lee et al. (2009) developed spin- and dip-coated linear polyethylenimine/poly (acrylic acid) films and, based on the investigations of the surface roughness and the relative composition of constituting polyelectrolytes, concluded that spin-coating films showed less polyelectrolytes interpenetration between the layers, producing a linear growth of the thickness, rather than the common exponential growth in the LbL assembly by dip-coating.

Furthermore, the presence of BGNPs on the dip- and spin-coated MF configurations seemed to contribute to lower color-mixed spots, in comparison with the dip- and spin-coated CTR configurations. This finding is quite relevant, indicating that the presence of BGNPs might act as barrier to the polyelectrolytes diffusion, promoting a more uniform polymeric layer deposition.

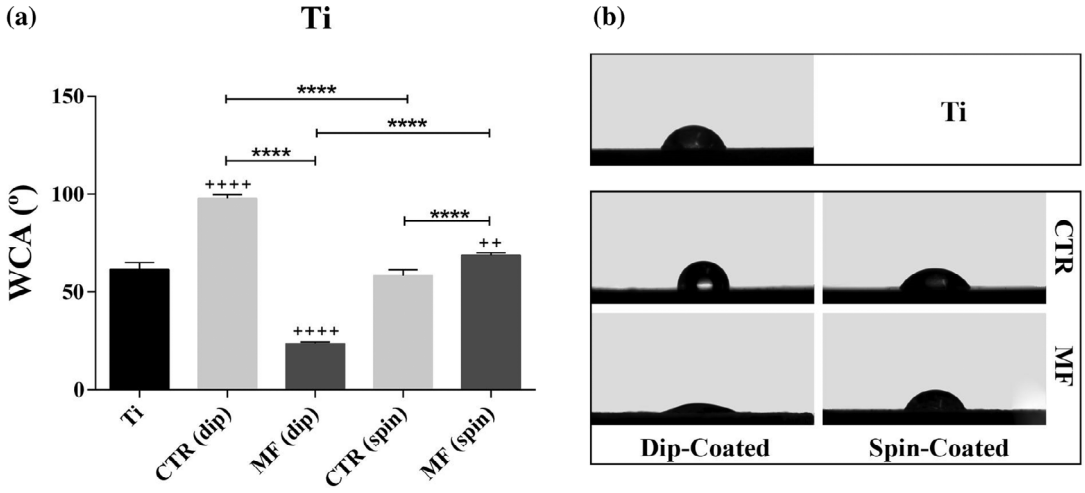

FIGURE 14 (a) WCA (°) values measured for the two LbL coatings configurations produced onto Ti by dip- and spin-coating. Statistical differences between the various configurations are indicated by "*," while their comparisons with the uncoated Ti substrate (Ti control) are indicated by "+" (at the top of each bar). Data are presented by means ± standard deviation (n = 3; ++++/**** p < .0001; ++ p < .01) (One-way ANOVA with Tukey's Multiple comparison test); (b) representative image of water drops for each multilayered film surface

For the metals, 316L SS and Ti (Figures 7 and 8), the results were not so clear. Besides the intensity differences that were observed between both LbL methods, representing differences on their surface roughness, a similar color mixture for dip- and spin-coated CTR conditions was noticed. Such finding could be related with the intrinsic surface roughness of these two metals, which can contribute to a higher polyelectrolytes interpenetration between the layers of the coatings. However, dip- and spin-coated MF films evidenced similar results to the glass substrate, also indicating that BGNPs acted as barrier to the polyelectrolytes diffusion, even with the higher surface roughness of the metals.

AFM analysis (Figures 9–11) also exhibited more significant topography results for LbL coatings produced onto glass. As it can be seen in Figure 9, spin-coated LbL films had lower roughness than the dip-coated ones. Marudova et al. (2016) also observed that spin-coated CHT/xanthan multilayer films are smoother than the dip-coated ones. The lower roughness of spin-coated coatings was attributed to a lack of polyelectrolytes interpenetration giving rise to more flat and clearly separated layers (Marudova et al., 2016). On the other hand, the rough surface topography of the dip-assembled coatings could indicate the presence of higher loose interpenetrating structures (Marudova et al., 2016).

Furthermore, Figure 9 revealed that the spin- and dip-coated MF films containing BGNPs had lower surface roughness compared to their respective controls. This can be explained by the combined effect of catechol groups from CHT-C and HA-C, which maintain the inorganic phase strongly bonded to the polymeric phase, acting as a glue (Neto et al., 2014; Rego et al., 2016).

On the other hand, both SS and Ti controls exhibited a high surface roughness (Figures 10 and 11). Hence, roughness differences between the substrates and LbL conditions were not significant. In general, the surface roughness of the LbL conditions tended to decrease, when compared to the SS and Ti control, which indicates that the coatings contributed to a higher uniformity of the substrates. A comparative study between dip- and spin-coating techniques found that the dip-assembly prepared thicker, rougher films, whereas spinning resulted in thinner and smoother films (Seo, Lutkenhaus, Kim, Hammond, & Char, 2008). However, in the present study, the metal substrates had a high surface roughness and, consequently, such differences between dip and spin coatings were not evident.

Furthermore, for both dip- and spin-coated MF films, the presence of BGNPs seemed to contribute to a higher surface roughness compared to their respective controls. These topographic results appeared to have a significant interference of the intrinsic metal surface roughness. Nevertheless, the present study is relevant since many metal implants have surface roughness superior or similar to the metallic substrates used in the present study. In fact, the roughness has a strong influence on the surface adhesion of living tissues. Particularly, the increase of the implant surface roughness has been used to enhance the bonding strength of living tissues, due to the higher specific surface area of the implant in the tissue-implant contact (Krishna Alla et al., 2011). Moreover, for Ti substrates, Chen et al. already demonstrated that multilayered coatings with higher surface roughness promoted improved osteoblasts adhesion, proliferation and differentiation (Chen et al., 2017).

As expected from the AFM analysis, WCA changes between the various LbL conditions and the uncoated substrates were noticed (Figures 12–14). According to the Wenzel model (Wenzel, 1949), roughness affects the contact angle hysteresis. This model predicts that roughness will decrease the WCA if the angle on the smoother surface of the same material is lower than 90° (hydrophilic solid). On the other hand, the WCA will increase if the angle is higher than 90° (hydrophobic solid) (Wenzel, 1949). Therefore, since the uncoated glass surface has a hydrophilic nature (WCA around 74°), the increased roughness of the dip-coated LbL conditions compared to

the spin-coated ones resulted in a WCA decrease. It was found that the coatings obtained by both LbL methods exhibit higher hydrophilicity than the glass control. These results can be related by the presence of the catechol groups in modified CHT and HA, since an hydrophilicity increase of the glass substrate after deposition of multilayer films containing catechol-modified HA was previously reported (Chen et al., 2017; Hong et al., 2013; Neto et al., 2014; Zhang, Li, Yuan, Cui, & Yang, 2013). Particularly, in a previous work developed by our group (Neto et al., 2014), $[CHT/HA\text{-}C]_{10}$ dip-coated films showed lower WCA values (around 73°) compared to $[CHT/HA]_{10}$ dip-coated films (around 77°), using glass as substrate. These WCA results obtained for $[CHT/HA\text{-}C]_{10}$ dip-coated films were higher than those obtained in the present study, and these finding could be explained by the higher content of catechol groups in the LbL coatings, as both polymers were modified with catechol groups. Furthermore, the inclusion of BGNPs in the dip- and spin-coated films appeared to affect their wettability. In fact, the presence of BGNPs in the MF films increased their hydrophilicity, in agreement with previous works (Caridade et al., 2013; Li, Shi, Dong, Zhang, & Zeng, 2008).

Similarly with the glass wettability results, an increase of the hydrophilicity of the SS substrates was observed with the film deposition by the two LbL methods (Figure 13). In particular, a more pronounced WCA decrease was found for both dip- and spin-coated MF conditions, when compared to their respective controls. This decrease was related to the hydrophilic nature of BGNPs and was statistically significant for both dip- and spin-coated MF conditions. Unlike glass, the uncoated SS substrate evidenced a hydrophobic nature (107°). According to the Wenzel model (Wenzel, 1949), the increased roughness will increase the WCA if the angle is higher than 90° (hydrophobic material) (Wenzel, 1949). Figure 13 evidenced significant higher WCA values for both spin-coated CTR and MF conditions, when compared to the dip-coated ones. In fact, it was previously noticed through AFM that the LbL conditions obtained by spin-coating seemed to present a higher surface roughness than those obtained by dip-coating.

For Ti, unlike the glass and SS wettability results, a WCA decrease was not detected for all conditions. Clearly, the Ti wettability results were influenced by its intrinsic surface roughness. Once again, according to the Wenzel model, since the uncoated Ti substrate showed a hydrophilic nature (about 61°), its greater roughness will decrease the WCA. For the dip-coated CTR condition a significant decrease in the hydrophilicity of the Ti substrate was found, when compared to the spin-coated one (Figure 14), which can be explained by the increased surface roughness of the spin-coated CTR. Since the spin-coating technique produces thinner films, the intrinsic roughness of the metal can more easily affect the wettability, showing WCA values similar to the Ti control. On the other hand, the dip-coated MF condition led to a significant hydrophilicity increase of the Ti substrate, when compared to the spin-coated one. Unlike the spin-coating method, dip-assembly led to a less homogeneous distribution of BGNPs that could contribute to an increase in the surface roughness of MF films.

5 | CONCLUSIONS

Dip- and spin-coating techniques were successfully applied for the deposition of catechol-modified polysaccharides multilayered films combining or not bioglass nanoparticles onto different substrates, glass, 316L SS and Ti foils. SEM images of all substrates evidenced that, at the microscale, the spin-coated formulations had a smoother and more homogeneous surface morphology than the dip-coated ones.

Further investigations with FT-IR imaging and AFM analysis revealed that both spin-coated films on the glass substrate had a more uniform structure with lower surface roughness, when compared to those obtained by dip-coating. These results could be interpreted as a lack of PE interpenetration between the spin-coated layers, unlike those obtained by dip-assembly.

For the glass substrate, it was found that the incorporation of BGNPs in both dip- and spin-coated films contributed to a smoother cohesive structure with less diffusion of PEs, when compared to their respective controls. Such feature could be a result from the combination of catechol groups of both CHT-C and HA-C polymers, acting as a glue between the inorganic and organic phase. Wettability analysis revealed that the coatings obtained by the two LbL methods exhibit higher hydrophilicity than the glass control. It was also found that the spin-coated films had higher WCA than the dip-coated ones. For both metallic foils (316L SS and Ti), such differences were not so obvious. This feature was due to the intrinsic surface nano-roughness observed by AFM for these two substrates. Nevertheless, from the FT-IR analysis, we noticed that although the results of MF condition on both metals are in agreement with those found for the glass substrate, the CTR condition presented a PE color-mixture for both LbL methods, evidencing PE layer interpenetration. Furthermore, unlike the AFM results of the glass, for both dip- and spin-coated MF films, the presence of BGNPs seemed to contribute to a higher surface roughness compared to their respective controls. In general, for both metals, the wettability increased when the coatings were deposited through both LbL methods. Attending the overall surface properties exhibited in the present work, the developed films revealed favorable features to be potentially used as versatile adhesive coatings of a variety of orthopedic implants.

ACKNOWLEDGMENTS

The authors acknowledge the Portuguese Foundation for Science and Technology (FCT) and the European program FEDER/FEEI for the financial support through projects PTDC/BTM-MAT/28123/2017 and PTDC/NAN-MAT/31036/2017 and to the European Commission Horizon 2020 programme under the following grant agreements: 692333-CHEM2NATURE, 668983-FORECAST, and 739572-THE DISCOVERIES CTR. The authors also acknowledge FCT for the financial support through the exploratory project MIT-EXPL/BIO/0089/2017. This article has also been prepared with the support of REMIX Project, funded by the European Union's Horizon 2020 Research and

Innovation programme under the Maria Sklodowska-Curie grant agreement n. 778078.

ORCID

Ana C. Vale https://orcid.org/0000-0002-1590-6636

Natália M. Alves https://orcid.org/0000-0002-8741-4091

REFERENCES

Altmaier, M., Kienzler, B., Montoya, V., Duro, L., & Grivé, M. (2012). *4th annual workshop proceedings of the collaborative project "redox phenomena controlling systems" (7th EC FP CP RECOSY)*. Karlsruhe, Germany: KIT Scientific Publishing.

Alves, N. M., Pashkuleva, I., Reis, R. L., & Mano, J. F. (2010). Controlling cell behavior through the design of polymer surfaces. *Small*, *6*(20), 2208–2220.

Baino, F., Novajra, G., Miguez-Pacheco, V., Boccaccini, A. R., & Vitale-Brovarone, C. (2016). Bioactive glasses: Special applications outside the skeletal system. *Journal of Non-Crystalline Solids*, *432*, 15–30.

Boccaccini, A. R., Erol, M., Stark, W. J., Mohn, D., Hong, Z., & Mano, J. F. (2010). Polymer/bioactive glass nanocomposites for biomedical applications: A review. *Composites Science and Technology*, *70*(13), 1764–1776.

Borges, J., & Mano, J. F. (2014). Molecular interactions driving the layer-by-layer assembly of multilayers. *Chemical Reviews*, *114*(18), 8883–8942.

Caridade, S. G., Merino, E. G., Alves, N. M., Bermudez, V. Z., Boccaccini, A. R., & Mano, J. F. (2013). Chitosan membranes containing micro or nano-size bioactive glass particles: Evolution of biomineralization followed by in situ dynamic mechanical analysis. *Journal of the Mechanical Behavior of Biomedical Materials*, *20*, 173–183.

Carvalho, A. L., Vale, A. C., Sousa, M. P., Barbosa, A. M., Torrado, E., Mano, J. F., & Alves, N. M. (2016). Antibacterial bioadhesive layer-by-layer coatings for orthopedic applications. *Journal of Materials Chemistry B*, *4*(32), 5385–5393.

Chen, W., Shen, X., Hu, Y., Xu, K., Ran, Q., Yu, Y., … Cai, K. (2017). Surface functionalization of titanium implants with chitosan-catechol conjugate for suppression of ROS-induced cells damage and improvement of osteogenesis. *Biomaterials*, *114*, 82–96.

Chien, C. Y., Liu, T. Y., Kuo, W. H., Wang, M. J., & Tsai, W. B. (2013). Dopamine-assisted immobilization of hydroxyapatite nanoparticles and RGD peptides to improve the osteoconductivity of titanium. *Journal of Biomedical Materials Research. Part A*, *101*(3), 740–747.

Chien, C.-Y., & Tsai, W.-B. (2013). Poly(dopamine)-assisted immobilization of Arg-Gly-asp peptides, hydroxyapatite, and bone Morphogenic Protein-2 on titanium to improve the osteogenesis of bone marrow stem cells. *ACS Applied Materials & Interfaces*, *5*(15), 6975–6983.

Cho, J., Char, K., Hong, J.-D., & Lee, K.-B. (2001). Fabrication of highly ordered multilayer films using a spin self-assembly method. *Advanced Materials*, *13*(14), 1076–1078.

De, M., Ghosh, P. S., & Rotello, V. M. (2008). Applications of nanoparticles in biology. *Advanced Materials*, *20*(22), 4225–4241.

de Villiers, M. M., Otto, D. P., Strydom, S. J., & Lvov, Y. M. (2011). Introduction to nanocoatings produced by layer-by-layer (LbL) self-assembly. *Advanced Drug Delivery Reviews*, *63*(9), 701–715.

Dupont, K. M., Boerckel, J. D., Stevens, H. Y., Diab, T., Kolambkar, Y. M., Takahata, M., … Guldberg, R. E. (2012). Synthetic scaffold coating with adeno-associated virus encoding BMP2 to promote endogenous bone repair. *Cell and Tissue Research*, *347*(3), 575–588.

Ghadban, A., Ahmed, A. S., Ping, Y., Ramos, R., Arfin, N., Cantaert, B., … Miserez, A. (2016). Bioinspired pH and magnetic responsive catechol-functionalized chitosan hydrogels with tunable elastic properties. *Chemical Communications*, *52*(4), 697–700.

Gittens, R. A., Olivares-Navarrete, R., Schwartz, Z., & Boyan, B. D. (2014). Implant osseointegration and the role of microroughness and nanostructures: Lessons for spine implants. *Acta Biomaterialia*, *10*(8), 3363–3371.

Goodman, S. B., Yao, Z., Keeney, M., & Yang, F. (2013). The future of biologic coatings for orthopaedic implants. *Biomaterials*, *34*(13), 3174–3183.

Gribova, V., Auzely-Velty, R., & Picart, C. (2012). Polyelectrolyte multilayer assemblies on materials surfaces: From cell adhesion to tissue engineering. *Chemistry of Materials*, *24*(5), 854–869.

Halasz, K., Grozdits, G., & Csóka, L. (2015). 10—Functional nanostructured coatings via layer-by-layer self-assembly. In M. Aliofkhazraei (Ed.), *Anti-abrasive nanocoatings* (pp. 249–281). Cambridge, England: Woodhead Publishing.

Herrera, M. A., Sirviö, J. A., Mathew, A. P., & Oksman, K. (2016). Environmental friendly and sustainable gas barrier on porous materials: Nanocellulose coatings prepared using spin- and dip-coating. *Materials and Design*, *93*, 19–25.

Hong, S., Yang, K., Kang, B., Lee, C., Song, I. T., Byun, E., … Lee, H. (2013). Hyaluronic acid catechol: A biopolymer exhibiting a pH-dependent adhesive or cohesive property for human neural stem cell engineering. *Advanced Functional Materials*, *23*(14), 1774–1780.

Hong, Z., Reis, R. L., & Mano, J. F. (2009). Preparation and in vitro characterization of novel bioactive glass ceramic nanoparticles. *Journal of Biomedical Materials Research. Part A*, *88*(2), 304–313.

Huang, X., Bao, X., Liu, Y., Wang, Z., & Hu, Q. (2017). Catechol-functional chitosan/silver nanoparticle composite as a highly effective antibacterial agent with species-specific mechanisms. *Scientific Reports*, *7*(1), 1860.

Jha, P. K., & Halada, G. P. (2011). The catalytic role of uranyl in formation of polycatechol complexes. *Chemistry Central Journal*, *5*, 12–12.

Jones, J. R. (2013). Review of bioactive glass: From Hench to hybrids. *Acta Biomaterialia*, *9*(1), 4457–4486.

Jones, J. R. (2015). Reprint of: Review of bioactive glass: From Hench to hybrids. *Acta Biomaterialia*, *23*(Suppl), S53–S82.

Kennedy, F., Rio, J., & Kuo, S. J. W. (2006). *Practical aspects of hyaluronan based medical products* (pp. 321–322). Boca Raton: CRC Press.

Kim, K., Kim, K., Ryu, J. H., & Lee, H. (2015). Chitosan-catechol: A polymer with long-lasting mucoadhesive properties. *Biomaterials*, *52*, 161–170.

Korn, P., Schulz, M. C., Hintze, V., Range, U., Mai, R., Eckelt, U., … Stadlinger, B. (2014). Chondroitin sulfate and sulfated hyaluronan-containing collagen coatings of titanium implants influence peri-implant bone formation in a minipig model. *Journal of Biomedical Materials Research. Part A*, *102*(7), 2334–2344.

Krishna Alla, R., Ginjupalli, K., Upadhya, N., Shammas, M., Krishna Ravi, R., & Sekhar, R. (2011). Surface roughness of implants: A review. *Trends in Biomaterials & Artificial Organs*, *25*(3), 112–118.

Kumar, T. S. (2013). *Physical and chemical characterization of biomaterials* (pp. 11–47). Cambridge, MA: Academic Press.

La, W. G., Jin, M., Park, S., Yoon, H. H., Jeong, G. J., Bhang, S. H., … Kim, B. S. (2014). Delivery of bone morphogenetic protein-2 and substance P using graphene oxide for bone regeneration. *International Journal of Nanomedicine*, *9*(Suppl. 1), 107–116.

Lawrie, G., Keen, I., Drew, B., Chandler-Temple, A., Rintoul, L., Fredericks, P., & Grondahl, L. (2007). Interactions between alginate and chitosan biopolymers characterized using FTIR and XPS. *Biomacromolecules*, *8*(8), 2533–2541.

Lee, H., Lee, Y., Statz, A. R., Rho, J., Park, T. G., & Messersmith, P. B. (2008). Substrate-independent layer-by-layer assembly by using mussel-adhesive-inspired polymers. *Advanced Materials*, *20*(9), 1619–1623.

Lee, H., Scherer, N. F., & Messersmith, P. B. (2006). Single-molecule mechanics of mussel adhesion. *Proceedings of the National Academy of Sciences of the United States of America*, *103*(35), 12999–13003.

Lee, Y. M., Park, D. K., Choe, W. S., Cho, S. M., Han, G. Y., Park, J., & Yoo, P. J. (2009). Spin-assembled layer-by-layer films of weakly charged polyelectrolyte multilayer. *Journal of Nanoscience and Nanotechnology*, *9*(12), 7467–7472.

Li, X., Shi, J., Dong, X., Zhang, L., & Zeng, H. (2008). A mesoporous bioactive glass/polycaprolactone composite scaffold and its bioactivity behavior. *Journal of Biomedial Materials Research Part A*, *84A*(1), 84–91.

Luz, G. M., & Mano, J. F. (2011). Preparation and characterization of bioactive glass nanoparticles prepared by sol–gel for biomedical applications. *Nanotechnology*, *22*(49), 494014.

Ma, J., Chen, C. Z., Wang, D. G., Meng, X. G., & Shi, J. Z. (2010). In vitro degradability and bioactivity of mesoporous CaO-MgO-P_2O_5-SiO_2 glasses synthesized by sol–gel method. *Journal of Sol–Gel Science and Technology*, *54*(1), 69–76.

Mačković, M., Hoppe, A., Detsch, R., Mohn, D., Stark, W. J., Spiecker, E., & Boccaccini, A. R. (2012). Bioactive glass (type 45S5) nanoparticles: in vitro reactivity on nanoscale and biocompatibility. *Journal of Nanoparticle Research*, *14*(7), 966.

Marudova, M., Bodurov, I., Sotirov, S., Uzunova, Y., Pilicheva, B., Avramova, I., … Yovcheva, T. (2016). Nanostructured polyelectrolyte multilayer drug delivery systems for buccal administration. *Bulgarian Chemical Communications*, *48*, 468–474.

Mohseni, E., Zalnezhad, E., & Bushroa, A. R. (2014). Comparative investigation on the adhesion of hydroxyapatite coating on Ti–6Al–4V implant: A review paper. *International Journal of Adhesion and Adhesives*, *48*, 238–257.

Neto, A. I., Cibrao, A. C., Correia, C. R., Carvalho, R. R., Luz, G. M., Ferrer, G. G., … Mano, J. F. (2014). Nanostructured polymeric coatings based on chitosan and dopamine-modified hyaluronic acid for biomedical applications. *Small*, *10*(12), 2459–2469.

Niinomi, M., Nakai, M., & Hieda, J. (2012). Development of new metallic alloys for biomedical applications. *Acta Biomaterialia*, *8*(11), 3888–3903.

Nyberg, E., Holmes, C., Witham, T., & Grayson, W. L. (2016). Growth factor-eluting technologies for bone tissue engineering. *Drug Delivery and Translational Research*, *6*(2), 184–194.

Peniche, C., Argüelles-Monal, W., Davidenko, N., Sastre, R., Gallardo, A., & San Román, J. (1999). Self-curing membranes of chitosan/PAA IPNs obtained by radical polymerization: Preparation, characterization and interpolymer complexation. *Biomaterials*, *20*(20), 1869–1878.

Rego, S. J., Vale, A. C., Luz, G. M., Mano, J. F., & Alves, N. M. (2016). Adhesive bioactive coatings inspired by sea life. *Langmuir*, *32*(2), 560–568.

Ryu, J. J., Park, K., Kim, H. S., Jeong, C. M., & Huh, J. B. (2013). Effects of anodized titanium with Arg-Gly-asp (RGD) peptide immobilized via chemical grafting or physical adsorption on bone cell adhesion and differentiation. *The International Journal of Oral & Maxillofacial Implants*, *28*(4), 963–972.

Sartori, M., Giavaresi, G., Parrilli, A., Ferrari, A., Aldini, N. N., Morra, M., … Fini, M. (2015). Collagen type I coating stimulates bone regeneration and osteointegration of titanium implants in the osteopenic rat. *International Orthopaedics*, *39*(10), 2041–2052.

Seo, J., Lutkenhaus, J. L., Kim, J., Hammond, P. T., & Char, K. (2008). Effect of the layer-by-layer (LbL) deposition method on the surface morphology and wetting behavior of hydrophobically modified PEO and PAA LbL films. *Langmuir*, *24*(15), 7995–8000.

Shah, N. J., Hyder, M. N., Quadir, M. A., Dorval Courchesne, N.-M., Seeherman, H. J., Nevins, M., … Hammond, P. T. (2014). Adaptive growth factor delivery from a polyelectrolyte coating promotes synergistic bone tissue repair and reconstruction. *Proceedings of the National Academy of Sciences*, *111*(35), 12847–12852.

Surmenev, R. A., Surmeneva, M. A., & Ivanova, A. A. (2014). Significance of calcium phosphate coatings for the enhancement of new bone osteogenesis—A review. *Acta Biomaterialia*, *10*(2), 557–579.

Tobin, E. J. (2017). Recent coating developments for combination devices in orthopedic and dental applications: A literature review. *Advanced Drug Delivery Reviews*, *112*, 88–100.

Wenzel, R. N. (1949). Surface roughness and contact angle. *The Journal of Physical and Colloid Chemistry*, *53*(9), 1466–1467.

Wilker, J. J. (2010). Marine bioinorganic materials: Mussels pumping iron. *Current Opinion in Chemical Biology*, *14*(2), 276–283.

Williams, R. (2011). *Surface modification of biomaterials: Methods analysis and applications* (pp. 1–415). Cambridge, UK: Woodhead Publishing.

Xiao, M., Chen, Y. M., Biao, M. N., Zhang, X. D., & Yang, B. C. (2017). Biofunctionalization of biomedical metals. *Materials Science & Engineering C: Materials for Biological Applications*, *70*(Pt 2, 1057–1070.

Xu, J., Strandman, S., Zhu, J. X. X., Barralet, J., & Cerruti, M. (2015). Genipin-crosslinked catechol-chitosan mucoadhesive hydrogels for buccal drug delivery. *Biomaterials*, *37*, 395–404.

Yu, M., & Deming, T. J. (1998). Synthetic polypeptide mimics of marine adhesives. *Macromolecules*, *31*(15), 4739–4745.

Zhang, X., Li, Z., Yuan, X., Cui, Z., & Yang, X. (2013). Fabrication of dopamine-modified hyaluronic acid/chitosan multilayers on titanium alloy by layer-by-layer self-assembly for promoting osteoblast growth. *Applied Surface Science*, *284*, 732–737.

SUPPORTING INFORMATION

Additional supporting information may be found online in the Supporting Information section at the end of this article.

How to cite this article: Almeida AC, Vale AC, Pires RA, Reis RL, Alves NM. Layer-by-layer films based on catechol-modified polysaccharides produced by dip- and spin-coating onto different substrates. *J Biomed Mater Res*. 2019;1–16. https://doi.org/10.1002/jbm.b.34489